Global dynamical network of the spatially correlated Pc2 wave response for the 2015 St. Patrick's Day storm

Shahbaz Chaudhry[1], Sandra C Chapman[1], Jesper W. Gjerloev[2], and Ciaran D Beggan[3]

[1]University of Warwick
[2]APL-JHU
[3]British Geological Survey

December 7, 2022

Abstract

We show the global dynamics of spatial cross-correlation of Pc2 wave activity can track the evolution of the 2015 St. Patrick's Day geomagnetic storm for an 8 hour time window around onset. The global spatially coherent response is tracked by forming a dynamical network from 1 second data using the full set of 100+ ground-based magnetometer stations collated by SuperMAG and Intermagnet. The pattern of spatial coherence is then captured by a few network parameters which in turn track the evolution of the storm. At onset IMF B_z>0 and Pc2 power increases, we find a global response with stations being correlated over both local and global distances. Following onset, whilst B_z>0, the network response is confined to the day-side. When IMF B_z<0, there is a strong local response at high latitudes, consistent with the onset of polar cap convection driven by day-side reconnection. The spatially coherent response as revealed by the network grows and is maximal when both SME and SMR peak, consistent with an active electrojet and ring-current. Throughout the storm there is a coherent response both in stations located along lines of constant geomagnetic longitude, between hemispheres, and across magnetic local time. The network does not simply track the average Pc2 wave power, however is characterized by network parameters which track the evolution of the storm. This is a first study to parameterize global Pc2 wave correlation and offers the possibility of statistical studies across multiple events to detailed comparison with, and validation of, space weather models.

Global dynamical network of the spatially correlated Pc2 wave response for the 2015 St. Patrick's Day storm

S.Chaudhry[1], S.C.Chapman[1,2], J.Gjerloev[3,4], C.D.Beggan[5]

[1]Centre for Fusion, Space and Astrophysics, Department of Physics, University of Warwick, Coventry, UK
[2]Department of Mathematics and Statistics, University of Tromso, Norway
[3]The Johns Hopkins University Applied Physics Laboratory, Laurel, Maryland, USA
[4]Department of Physics and Technology, University of Bergen, Bergen, Norway
[5]British Geological Survey, Edinburgh, UK

Key Points:

- First global network analysis of Pc2 wave activity using 100+ magnetometers at 1 second cadence
- Novel method to construct the dynamical network of globally coherent Pc2 wave activity
- Network parameters reveal the global magnetospheric response in the 2015 St. Patrick's Day storm

Corresponding author: Shahbaz Chaudhry, `shahbaz.chaudhry@warwick.ac.uk`

Abstract

We show the global dynamics of spatial cross-correlation of Pc2 wave activity can track the evolution of the 2015 St. Patrick's Day geomagnetic storm for an 8 hour time window around onset. The global spatially coherent response is tracked by forming a dynamical network from 1 second data using the full set of 100+ ground-based magnetometer stations collated by SuperMAG and Intermagnet. The pattern of spatial coherence is then captured by a few network parameters which in turn track the evolution of the storm. At onset IMF $B_z > 0$ and Pc2 power increases, we find a global response with stations being correlated over both local and global distances. Following onset, whilst $B_z > 0$, the network response is confined to the day-side. When IMF $B_z < 0$, there is a strong local response at high latitudes, consistent with the onset of polar cap convection driven by day-side reconnection. The spatially coherent response as revealed by the network grows and is maximal when both SME and SMR peak, consistent with an active electrojet and ring-current. Throughout the storm there is a coherent response both in stations located along lines of constant geomagnetic longitude, between hemispheres, and across magnetic local time. The network does not simply track the average Pc2 wave power, however is characterized by network parameters which track the evolution of the storm. This is a first study to parameterize global Pc2 wave correlation and offers the possibility of statistical studies across multiple events to detailed comparison with, and validation of, space weather models.

Plain Language Summary

Space weather poses a risk to infrastructure including satellites and power systems. A key challenge within space weather is predicting the magnetospheric response. To better understand geomagnetic activity, we (for the first time) build a dynamical network to parameterize the Pc2 wave response. Closed magnetic field lines in the inner magnetosphere can support standing Alfven waves (a magnetic 'harp') and these are measured on the ground as Pc waves which occupy distinct frequency bands. Pc waves are excited by a variety of processes related to space weather. Previous work has focused on chains of magnetometers that are at constant magnetic longitude which sample the different resonant frequencies of the 'harp' (different field line lengths). Recently, SuperMAG has begun to offer second resolution data which allows higher frequency Pc2 waves to be resolved and studied globally. Our first results are a study of an intense isolated geomagnetic storm where we have identified network parameters and have shown that these track the distinct phases of the storm in terms of spatial coherence of Pc2 wave activity. Using these network parameters we can perform statistical studies across many storms and quantitatively benchmark space weather models with observations.

1 Introduction

Reconfiguration of solar coronal field-lines can lead to an energetic release of plasma known as a coronal mass ejection (CME) (Schwenn, 2006). If the CME is incident on the magnetosphere with interplanetary magnetic field (IMF) $B_z < -10$nT and duration $t > 3$ h, an extreme space weather events known as a geomagnetic storm is induced (Gonzalez et al., 1994; Pulkkinen, 2007). In order to understand the dynamics of geomagnetic storms, we can study ultra low frequency (ULF) waves which are field line resonances (FLR) along closed field lines in the inner magnetosphere (Baumjohann & Treumann, 2012; McPherron et al., 1972; Hughes, 2013; Southwood & Hughes, 1983). During a storm there are a number of driving forces, both internal (magnetospheric) and external (solar wind), that can give rise to ULF waves. External ULF wave drivers include shear flow between the magnetosphere and the solar wind (McPherron et al., 1972; Yumoto, 1988) and the rapid displacement of field lines during the storm sudden commencement (SSC). When measured using ground-based magnetometers, ULF waves are classified as Pc waves

and occupy distinct frequency bands (Jacobs et al., 1964). There is extensive literature on the spatially localized physics of Pc waves (Rasinkangas et al., 1994; Chisham & Orr, 1997; Arnoldy et al., 1996) revealing that there are multiple physical processes during geomagnetic storms that can be measured using Pc waves. We focus on the Pc2 frequency band, for which generation mechanisms include ion-cyclotron resonance at equatorial regions of the magnetosphere (Kozyra et al., 1997; Murphy et al., 2014). Hence Pc2 waves are effective at depleting relativistic electrons from the outer radiation belts and ring current, leading to redistribution of plasma along field lines and thus modulating the duration of geomagnetic storms (Engebretson et al., 2008; Menk, 2011).

In this paper we study Pc2 wave excitation as a globally coherent phenomenon. We analyse an 8 hour time window around onset for the well known St. Patrick's Day event on the 17th of March 2015 (Wu et al., 2016a). Previous work has detailed the ionospheric effect of the storm (Mahrous et al., 2018; Maurya et al., 2018), electron precipitation from the radiation belts (Clilverd et al., 2020) and observations of global navigation satellite system (GNSS) disturbances (Jacobsen & Andalsvik, 2016). To analyse the global spatial correlation of Pc2 wave activity we create networks. First used in discrete mathematics, networks have become a useful tool in dynamical systems and have been used extensively in fields such as ecology, control systems, and particle physics (Strogatz, 2001; Newman, 2018). Dynamical network structure and evolution can be used to parameterize the system and underlying processes (Boccaletti et al., 2006). In geophysics, networks have been used to characterize ionospheric total electron content (McGranaghan et al., 2017), ground induced current in response to storms (Orr, Chapman, & Beggan, 2021) and substorm ionospheric current systems (Orr, Chapman, Gjerloev, & Guo, 2021).

The time dependent network will be built from observations using the full set of 100+ globally distributed ground-based magnetometer stations, curated by the Super-MAG/Intermagnet collaborations. Networks have been previously used successfully with 1 minute resolution SuperMAG data to obtain the timings of the high latitude response to IMF B_z turnings (Dods et al., 2017) and the evolution of high latitude current systems during substorms (Dods et al., 2015; Orr et al., 2019; Orr, Chapman, Gjerloev, & Guo, 2021). For the first time we perform network analysis with 1 second high resolution data using Pc2 waves. Our analysis demonstrates that Pc2 wave cross-correlation between globally spatially distributed observations can track the evolution of the storm in terms of evolving physical processes. The Pc2 wave band is optimal because the frequency is low enough to be well resolved by 1 second measurements, and high enough to have a relatively short cross-correlation time window. Therefore, we build dynamical Pc2 networks to chart the time evolution of full spatio-temporal pattern of coherence under active conditions. The Pc2 / Pi2 band has also been studied extensively both in terms of the basic physics and also as an indicator for processes taking place in the magnetosphere/ionosphere system (Kitamura et al., 1988).

To build Pc2 dynamical networks, we first band-pass filter ground magnetometer data and then use the filtered waveforms to build a time-varying matrix of cross-correlation between all pairs of ground stations. Thresholding this matrix provides a set of network connections between stations, providing a network for each component of the magnetic field. We construct random surrogates of the data to determine the statistical significance of the networks. We find that the Pc2 in-phase undirected networks are statistically significant over most of the event and hence we focus on these. Finally we parameterize the global spatio-temporal correlation patterns using a few network parameters.

The paper is organized as follows. Section 2 summarizes the event studied, the available data and the methodology for constructing the network which is detailed in Appendix, section A. The network parameters that characterize specific spatial properties of the networks, are introduced. Results in section 3 show how these network parameters characterize the time-evolution of the St. Patrick's Day storm. We conclude these results in Section 4.

2 Methods

2.1 Geomagnetic Storms and Data

We focus on the 2015 St. Patrick's Day event (Wu et al., 2016b) which occurred on the 17th of March 2015. The time-dependent network for this event are constructed from the full set of 128 ground magnetic field observations with 1 second cadence, curated by the SuperMAG and Intermagnet ground magnetometer collaborations. For our analysis we use the SuperMAG data calibration, ensuring magnetometer data have been preprocessed identically and allowing for multi-event and single event statistical analyses (Gjerloev, 2012). The vector time series for our data are given in coordinates where $\hat{n}$ is local magnetic north, $\hat{e}$ is local magnetic east and $\hat{z}$ is vertically down.

The 2015 St. Patrick's Day storm is the largest geomagnetic storm to date of solar cycle 24 (Li et al., 2017), classified as 'Severe' on the NOAA geomagnetic storm scale (Poppe, 2000; Jacobsen & Andalsvik, 2016). The onset or storm sudden commencement (SSC) occurred around 04:45 UT on 17 March, when a CME reached the Earth. Initially, the IMF B_z component was northward, reaching ∼27 nT at storm sudden commencement, then turned southward at around 06:00 UT. The storm reached its peak intensity at sim 00:00 UT on 18 March with minimum disturbance storm time index (Dst), sim -223 nT and had recovered (reaching background) by the 25th of March (Nosé et al., 2012; Wu et al., 2016b).

The dynamical Pc2 wave network of spatial cross-correlation is obtained over an 8 hour time window starting just before onset at 4:00 UT and ending at 12:00 UT, on the 17th of March.

2.2 Building a Dynamical Pc Wave Cross-correlation Network

A network graphs the connections (edges) between entities (nodes). Examples include social media networks, where the nodes are people and the edges are friendships between them, and airline networks, where the nodes are airports and the edges are flight paths (Newman, 2018). Network edges can be directed (flight path) or undirected, and have connections with different weights. In a dynamical network, both the available nodes, and the connections between them, are time-varying. Here, the network will be built upon the cross-correlation between the observed magnetic field at pairs of ground-based magnetometer stations. A pair of stations are connected when the cross-correlation estimated in a moving time window exceeds a fixed threshold. For real-world systems, the appropriate threshold is uniquely determined for each application. Key properties of the network can be captured by time-varying network parameters, which then track the evolution of the geomagnetic storm in terms of cross-correlation between spatially distributed stations. This study extends previous work that used 1 minute data (Dods et al., 2015, 2017; Orr et al., 2019; Orr, Chapman, Gjerloev, & Guo, 2021) to high resolution (1 second) SuperMAG and Intermagnet data applied to Pc2 waves.

A detailed description of how the network is constructed is given in the appendix, and is summarized here. Each magnetometer time series is sampled using a moving 100 seconds long time window which is 10 times the largest Pc2 wave period. Consecutive windows overlap by half the window size (50 seconds). The Pc2 waveforms are the extracted by band-pass filtering the windowed time series of each magnetometer. The two waveforms from pairs of magnetometers are then cross-correlated using a normalized time-lagged-cross-correlation (TLCC, see appendix A1). Next, a peak finding routine determines all positive and negative extrema of the TLCC function (which oscillates about zero) and gives the amplitude of the peak closest to zero lag, A_{p_0} occurring at lag τ_{p_0}. If A_{p_0} is above a threshold such that the $|A_{p_0}| > 0.3$, the station pair are connected in the network. This threshold was estimated by modelling (see Appendix A.2). This

168 procedure is repeated for all station pairs in each time window to generate the network,
169 for more detail see the Appendix, section A2.

170   Each network edge falls into one of three categories depending on A_{p_0} and τ_{p_0}: (i)
171 undirected in-phase, if $|\tau_{p_0}| \leq 1$ and $A_{p_0} > 0$. (ii) Undirected anti-phase, if $|\tau_{p_0}| \leq$
172 1 and $A_{p_0} < 0$. (iii) Directed, if $|\tau_{p_0}| > 1$. These categories correspond to three dis-
173 tinct networks, in section 3 we will focus on the undirected in-phase network, and ex-
174 amples from the anti-phase undirected networks are given in the Appendix, section B.

175   For each network category there will then be a network for each magnetic field com-
176 ponent, $\hat{e}$, $\hat{n}$, and $\hat{z}$, where $\hat{n}$ is local magnetic north, $\hat{e}$ is local magnetic east and $\hat{z}$ is
177 vertically down (Newell & Gjerloev, 2012).

178   To test the statistical significance of the networks we will compare our analysis to
179 a Pc2 surrogate dynamical network (Schreiber & Schmitz, 2000). We construct surro-
180 gate time series in order to test against the null hypothesis of no coherent phase infor-
181 mation. For each pair of stations, one Pc2 waveform is randomly shuffled, and the other
182 Pc2 waveform is unchanged. The full network analysis is then performed on this surro-
183 gate pair to give a randomized surrogate network. The number of connections in each
184 network divided by the number in the randomized surrogate to then provide an estimate
185 of the signal to noise ratio $\phi_k(t)$, for each field component $k = \hat{n}, \hat{e}, \hat{z}$ at time, t.

2.3 Sub-Networks and Network Parameters

187   The overall evolution of each network can be tracked with network parameters, which
188 in turn track different aspects of the evolution of the storm. These parameters will be
189 defined for the networks for each magnetic field component, $k = \hat{n}, \hat{e}, \hat{z}$. Sub-networks,
190 that is, subsets of the connections within the network, track different geographical and
191 physical aspects of the magnetospheric is response to the storm. Ratios of the number
192 of connections in these sub-networks then parameterize the network structure.

193   The number of connections in each of the sub-networks is as follows:

194   • **Overall level of global activity,** $\theta_k(t)$: The total number of connections in the
195   network, normalized to the total possible number of connections.
196   • **Localized in longitude,** $C_k(t)$: Number of connections between stations within
197   two degrees of magnetic longitude are referred to here as being part of the same
198   magnetometer 'pseudo-chain', these signify resonance between different L-shells.
199   Magnetometer pseudo-chains can be within or between hemispheres. Magnetome-
200   ter pseudo-chains have historically been used for Pc wave studies (Ziesolleck & Mc-
201   Diarmid, 1994; Chisham & Orr, 1997; Rasinkangas et al., 1994). We examined the
202   stricter condition of magnetic conjugacy for resonance along a single field line. How-
203   ever only two conjugate station pairs were found, compared with the 99 station
204   pairs which could exhibit cross-correlation with one other station at the same mag-
205   netic longitude.
206   • **Globally resonant L-shells,** $G_k(t)$: The number of connections between sta-
207   tions in the geomagnetic northern and southern hemispheres. There are 29 sta-
208   tions in the southern hemisphere out of the 128 stations in total.
209   • **Short-range ($S_k(t)$) vs long-range ($L_k(t)$) in magnetic local time (MLT)**:
210   The number of connections spanning MLT<4 h are denoted as $S_k(t)$ and MLT>4
211   h as $L_k(t)$. Any sub-network of multiple short-range connections will preferentially
212   be found on spatial scales with MLT<4 h, and as such can only exist within con-
213   tinental scales, that is, over a land-mass that is well populated by ground based
214   magnetometers. Long-range connections on the other hand can be ocean-spanning
215   and reach between continents. This network parameter then discriminates between
216   these two distinct classes of network connection.

The extent in MLT is chosen such that it approximately corresponds to continental scales. We anticipate a local response to be dominated by the high density of magnetometers, here in North America and Canada.

- **Within the northern hemisphere, $N_k(t)$:** A regionally localized response on a single hemisphere will respond to high latitude convection and current systems. We focus on connections limited in extent to the geomagnetic northern hemisphere as it is more extensively sampled.

The number of connections in each of these sub-networks is plotted as a function of time in Figure 1, and their ratios, the network parameters, are plotted in Figure 2.

3 Results

We first detail the timeline of the 2015 St. Patrick's Day storm and identify the time intervals when there is a statistically significant network response, in section 3.1. We then present the detailed network response as seen in the timeline of the storm and provide detailed snapshots of the network at key times in section 3.2. As discussed above, we found that the dominant network is for the in-phase undirected network for the $\hat{n}$ component. At peak, this network has ~ 5000 connections compared to the the ~ 1000 connections in the $\hat{e}, \hat{z}$ in-phase undirected networks. The $\hat{n}$ undirected in-phase network is above the signal to noise ratio $\phi_n > 2$ throughout the event. Therefore, we focus on the undirected in-phase network $\hat{n}$ component, and the $\hat{e}$, $\hat{z}$ components when $\phi_{e,z} > 2$. The sub-networks and network parameters for the $\hat{n}$, $\hat{e}$, and $\hat{z}$ magnetic field components do not necessarily track each other, or the Pc2 wave power.

3.1 Time Evolution of the Event

Figures 1 and 2 provide an overview of the storm, and the network parameter response. The format of these figures is as follows. Panel (a) summarizes the solar wind driving and panel (b) the overall magnetospheric response. The vertical lines indicate times (T1-6) which sample each phase of the storm, for which we will plot snapshots of the detailed network response in figures 3-8. Panel (c) plots the average Pc2 wave power over all magnetometer stations and the normalized total number of connections θ_k for $k = \hat{n}, \hat{e}, \hat{z}$. Panel (d) plots the signal to noise ratio ϕ_k constructed as detailed in section 2. A black horizontal line indicates $\phi_k = 2$ above which the number of network connections significantly exceeds that seen in the surrogate time series. We have set the threshold for significant Pc wave activity relative to the level seen before onset, as detailed in Appendix A. Before onset, the number of network connections is therefore low, (<100) so that ϕ_k fluctuates rapidly about this threshold. The first strong network response is seen at onset.

The phases of the storm, and the overall response of the network, are shown in figure 1 and are as follows:

- **T1, onset at 04:47:50 UT**: We see that IMF B_z increases to $\sim +27$ nT in panel (a) as we see a sharp increase in SME and SMR by MLT in panel (b). However, the dynamic pressure applied by the solar wind (panel (a), black line) increases shortly after at 5:00 UT. Network connections for the $\hat{n}$ and $\hat{e}$ components become significant as $\phi_n \approx 4$ and $\phi_e \approx 2.8$, while ϕ_z is just on the threshold. There is a sharp spike in all sub-networks.
- **T2, within 04:47:50 - 06:00:00 UT**: There is a day-side response with solar wind driven compression and IMF $B_z > 0$. Between T1 and T2 $\phi_n \approx 4$, a significant response in the $\hat{n}$ component of the magnetic field. The network response in the other components is not strongly significant, as there is a low number of connections (<100) in these networks.

- **T3, within 06:00-06:45 UT**: The IMF turns southward at 06:00 UT and there is an interval of $B_z < 0$. This can be expected to drive polar cap convection and we see a high latitude response begin in SME. All magnetic component sub-network connections increase after 06:10-06:20 UT, and now all components are statistically significant, $\phi_{n,e,z} > 2$. This 10-20 min delay is consistent with that found previously for the ionospheric response to a southward turning of the IMF (Todd et al., 1988; Dods et al., 2017).
- **T4, 06:47:00 UT**: IMF B_z turns toward zero and is approximately zero at T4 where the Pc2 wave power peaks and all components remain statistically significant, $\phi_{n,e,z} > 2$. The sub-network responses peaked earlier than the Pc2 wave power, instead tracking the increase in SME and levels out then decreases to a minimum about 20 minutes after the IMF reaches zero (however there is a data gap in the IMF after T4).
- **T5-T6, between 08:17:00 - 09:15:00 UT**: All magnetic component network connections increase and remain statistically significant, while SME increases and SMR decreases. All sub-network responses and Pc2 wave power peaks and the maximum excursion of SME and SMR. This is where magnetospheric and ionospheric current systems are responding most strongly to the storm. However, the network response, particularly for the $\hat{n}$ component of the field, starts to increase at T5 which is before the Pc2 wave power starts to increase, about an hour before the peak in Pc2 wave power.

Figure 1 shows that the in-phase instantaneous (close to zero cross-correlation lag) connections show a statistically significant network response compared to the randomized surrogate, throughout the event. Anti-phase connections are significant within subintervals for this event, and they are shown in Appendix B in figures B1 and B2. The anti-phase networks do not contribute to significant additional overall parameterization of the storm.

3.2 Detailed Network Response, Network Parameters

Figure 2 panels (e-i) plot the network parameters, that is, ratios of the number of connections in the sub-networks from figure 1. Snapshots of the networks at times T1-6 are plotted for the $\hat{n}$ magnetic field component network in figures 3-8. Snapshots for the $\hat{e}$ and $\hat{z}$ component networks are given in the Appendix section C, where these networks have different behaviour and are statistically significant. The network snapshots plot all connections (green) and three of the sub-networks: (i) localized in MLT (orange), (ii) localized in MLT and between the geomagnetic north and southern hemispheres (purple), (iii) along lines of fixed MLT (blue) showing magnetometer pseudo-chain connections which include magnetically conjugate connections. In figures 3-8, panels (a) and (c) show the connections within each hemisphere, panel (d) shows all connections in geomagnetic coordinates, and panel (b) the degree distributions of the sub-networks (i-iii). Long range connections are limited in extent to MLT≤ 12. The nodes (magnetometer stations) are indicated by red circles in all panels. In figures 3-8 the node size is scaled by the total number connections at that node. Black nodes plot magnetometer stations that are not part of the network (no significant station-station cross-correlation).

The spatial coverage of magnetometer stations is not uniformly distributed, so that sampling varies with MLT. At storm onset North America/Canada is initially located between dusk and close to midnight, while Europe is initially near dawn and Australia/East-Asia is just after noon. Europe then moves to the day-side while Australia/-East-Asia moves towards dusk, and North America/Canada moves through the night-side. Europe is dominated by the EMMA chain and Australia/East-Asia dominated by the MAGDAS chain. Multiple chains are located across North America. Therefore, we expect to see a night-side response (auroral electrojet) in North America/Canada, with a day-side re-

sponse initially at Australia/East-Asia and then in Europe. The short-range MLT (orange/purple) and pseudo-chains (blue) connections will be dominated by these continental groups of magnetometers. The network snapshots (figures 3-8) can give us a unique overview of how these different magnetometer groups are responding within and between each geographical region.

We now detail the in-phase network dynamics of the 2015 St. Patrick's Day storm using network parameters in figure 2 (for significant components) which we compare to network snapshots in figures 3-8 for the $\hat{n}$ component for each time, T1-6.

T1 onset, IMF $B_z > 0$, Pc2 power peak

Network parameters (Figure 2): Geomagnetic indices SMR and SME spike (panel (b)) due to the pressure pulse from the solar wind, as does the Pc2 wave power and network response. There is a rapid increase in north-south connections relative to magnetometer pseudo-chains and northern hemisphere connections $G_{n,e}/C_{n,e} > 1$, $G_{n,e}/N_{n,e} > 1$ in panels (f) and (g). We also see that long-range connections dominate short-range connections with $L_{n,e}/S_{n,e} > 1$, indicating a global response, shown in panels (i) and (j). This confirms that the enhancement in SME is due to the sudden commencement of the storm, rather than an electrojet response. We also see that north-south ($G_{n,e}$) connections are enhanced as $B_z > 0$ showing global L-shell resonance due to the solar wind pressure pulse and shear flow at the flanks.

Network snapshot (Figure 3): A global response is seen with long-range connections across the globe and short-range MLT connections excited in all three magnetometer groups. There are relatively more connections on the day-side (hence connected nodes) and at all latitudes. On the night-side there are more connections at higher latitudes (>30 degrees) with a corresponding gap in yellow connections between 0-6 h in MLT. Pseudo-chains are excited, particularly on the day-side, including two conjugate connections one on the day-side and one on the night-side. The degree distributions in panel (d) show that sub-networks are distributed broadly and are peaked showing distinct populations. Overall the network response is consistent with sharp day-side compression of the magnetosphere.

T2, between 04:47:50 - 06:00:00 UT, IMF $B_z > 0$

Network parameters (Figure 2): The number of north-south connections continues to exceed the number of magnetometer chain and northern hemisphere connections G_n/C_n, G_n/N_n both > 1 in panels (f) and (g). At this time Long-range connections continue to dominate short-range connections, $L_n/S_n > 1$, panels (i) and (j).

Network snapshot (Figure 4): There are fewer stations in the network overall. Short range MLT connections and pseudo-chains are mainly on the day-side with only one chain excited in Canada. Most low latitude connections are on the day-side including Antarctic stations. North-south hemisphere connections remain elevated because of a day-side cluster (between 30 degrees N and 60 degrees S). The degree distributions in panel (d) show all populations shifted towards the left and narrowed, now having lower average degree values. The network response is consistent with day-side compression and $B_z > 0$, it is still the sudden commencement phase.

T3, between 06:00 - 06:45 UT, IMF $B_z < 0$ to $B_z \approx 0$

Network parameters (Figure 2): During this time SME starts to increase, consistent with the onset of polar cap convection now B_z and B_y IMF are negative. As above, the detailed network response lags the IMF southward turning by approximately 15-20 minutes. The parameter $N_{n,e}/G_{n,e} > 1$ shows an increase in the number of northern hemisphere connections with the $\hat{e}$ component showing the greatest response. Magnetometer pseudo-chains (relative to north/south hemisphere connections) $C_{n,e}/G_{n,e} \approx 0.1, 0.3$

become enhanced, dominated by magnetometers in North America/Canada on the nightside. The local response is highlighted by short-range connections in MLT becoming dominant for the $\hat{e}$ component ($S_e/L_e > 1$). Long-range connections in MLT still persist in the $\hat{n}$ component with $L_n/S_n > 1$. *Network snapshot (Figure 5)*: The number of connections in the network has increased and we see degree distributions shifted to the right with higher average degree in panel (d). There are more network connections both within and between high latitude stations on the dusk side, consistent with enhanced dusk side polar cap convection under conditions of IMF $B_y < 0$. Multiple pseudo-chains are now excited in North America/Canada and there is a single conjugate connection between the North and South Pole, while on the South Pole only a single chain is excited. The network response here shows increasing connections both across MLT and across north and south hemispheres within a 4 h range of MLT, consistent with enhanced convection that is globally correlated during this interval of IMF $B_z < 0$ enhancing convection.

T4, 06:47 UT, IMF $B_z \approx 0$, Pc2 power peak

Network parameters (Figure 2): At this time IMF $B_z \approx 0$, SME is at a similar level to T3, and the Pc2 power is enhanced. We see the number of long-range and short-range connections are similar as $L_n/S_n \approx 1$ while $L_z/S_z > 1$, panels (i) and (j). Northern hemisphere connections for the $\hat{e}$ component continue to be enhanced relative to all other connections. The compressional component $\hat{z}$ shows an increase in the relative number of northern hemisphere connections which peaks at $G_z/C_z \approx 100$ in panels (e) and (f).

Network snapshot (Figure 6): We see that Pc2 power reaches a similar value to that at T1, however this time we see a predominately localized high latitude response at North America between 60N and 90N which highlights that the network response does not simply track Pc2 power. Pseudo-chains between hemispheres are mainly on the day-side, with few pseudo-chains excited on north-America and a single chain on the South Pole. There are more MLT<4 north-south connections on the dusk-side. The degree distribution here is similar to that of T3. Overall the network response at this time is consistent with enhanced high latitude currents during SME enhancement.

T5, 08:17 UT

Network parameters (Figure 2): Values for SMR by MLT become more negative and SME increases to ≈ 1000. There is a sharp peak in parameters C_n/G_n and N_n/G_n which reach values ~0.5 and ~10 respectively, in panels (e) and (h). These parameters indicate that network activity is becoming more localized in the northern hemisphere. This is the time when the network response for the $\hat{n}$ component of the magnetic field, starts to increase, about an hour before the peak in Pc2 wave power.

Network snapshot (Figure 7): Most connections are on the night-side at latitudes >60N, consistent with high latitude ionospheric currents, such as the auroral electrojet. Excited nodes are predominantly on the night-side and a few night-side pseudo-chains are also excited. The sparsity of connections between the north and south hemispheres is also reflected in the degree distributions, panel (d).

T6, between 09:15 - 12:00 UT, IMF $B_z < 0$ to $B_z > 0$, Pc2 power peak

Network parameters (Figure 2): Enhanced magnetospheric convection resumes as IMF $B_z < 0$ while SME and Pc2 power peaks as SMR by MLT is close to minimum. At this time long-range connections dominate with $L_n/S_n > 1$ and the total number of connections Θ_n peaks indicating a global response. Later, at 09:50 UT convection slows as $B_z \approx 0$ and we see the compressional component (magnetic $\hat{z}$ component) parameters peak with $N_z/G_z \approx 15$ and $C_z/G_z \approx 2$ shown in panels (e) and (h). Next, B_z spikes reaching +17 nT at 10:30 UT as more north-south connections are seen when $G_n/N_n > 1$ and $L_n/S_n \approx 2.3$ reaching maximum at 11:05 UT, showing a global response similar to T1. Large fluctuations in B_y coincide with a peak in $C_e/G_e \approx 0.6$ at 11:30 UT.

At this time there is no peak for N_e/G_e indicating that more magnetometer pseudo-chains are excited outside of the northern hemisphere unlike previously seen at times T3 and T4.

Network snapshot (Figure 8): We now have the peak of excitation, with activity at all latitudes. Pseudo-chains are excited in all MLT zones, noon-dusk, dusk-midnight, midnight-dawn, and dawn-noon. The two conjugate connections are on the day and night-side. There are more connections, in particular N-S connections and short-range connections at high latitudes, located in the region between midnight and dusk compared the region between midnight and dawn. Again this could simply reflect the available station coverage, but is also consistent with enhanced polar cap convection on the dusk side under conditions of IMF $B_y < 0$ (Moen et al., 2015). At this time we see the network is the most highly connected as the degree distributions become broader and has the highest average degree. In the degree distributions these distinct populations can be clearly seen for connections limited to MLT<4.
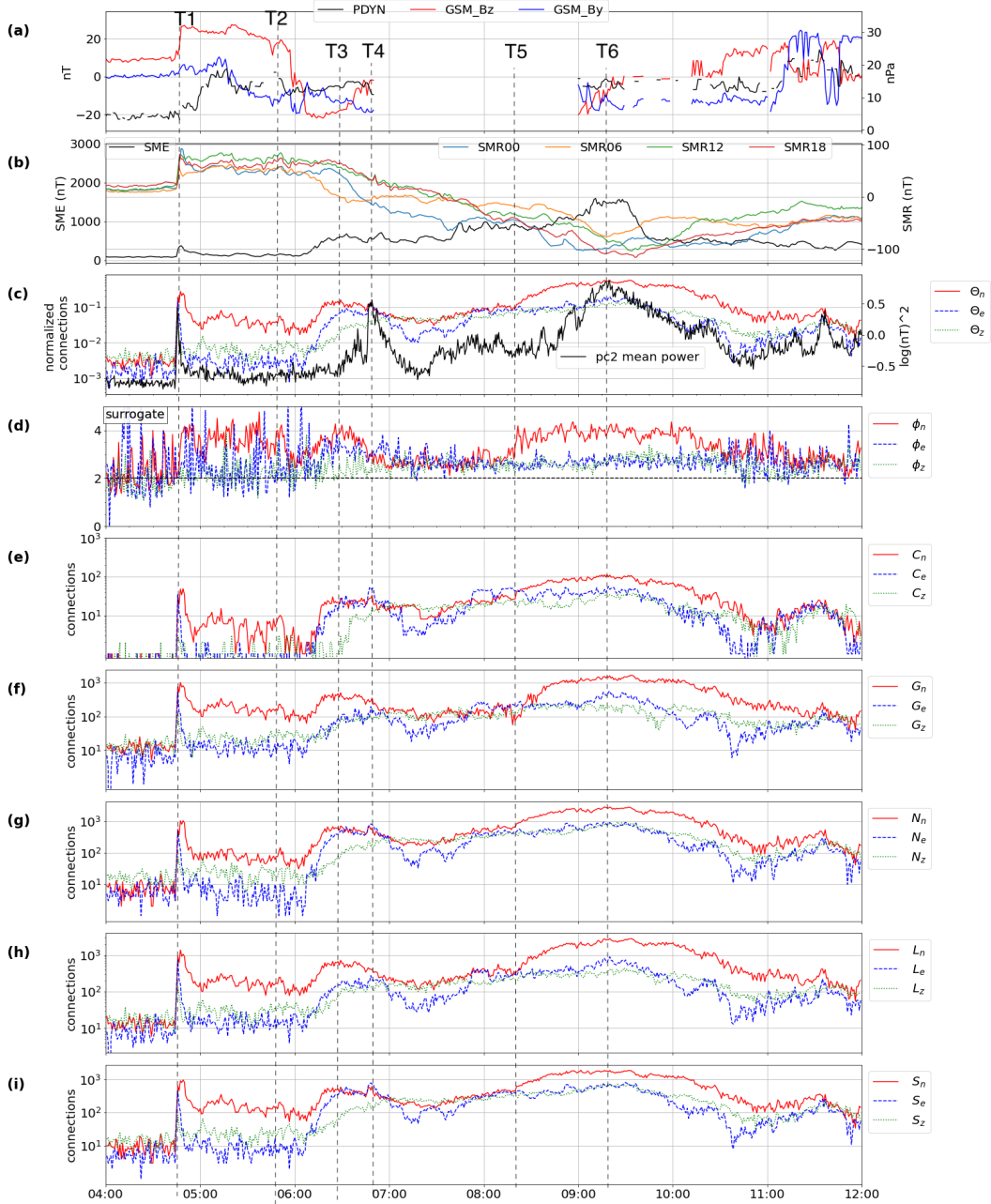
Figure 1: **Event overview and sub-networks.** Panel (a), solar wind parameters, dynamic pressure (PDYN in black), GSM IMF B_z (red), and B_y (blue) with data gap in OMNI data between *sim* 6:55-9:00 UT. Panel (b), geomagnetic indices SME and SMR by MLT region. Panel (c), mean Pc2 power along with the normalized total connection number Θ_k for $k = \hat{n}, \hat{e}, \hat{z}$ (red, blue and green) magnetic field components. Panel (d), signal to noise (surrogate) ratio ϕ_k with a black line at $\phi_k = 2$ above which is the threshold of statistical significance. Panel (e), the number of connections in a magnetometer chain (C_k). Panels (f) and (g), the number of connections in the geomagnetic northern hemisphere (N_k) and connections between the geomagnetic northern and southern hemispheres (G_k). Panels (h) and (i), connections less than 4 h in MLT (S_k) and greater than 4 h in MLT (L_k). Reference times are labelled T1-6 for which network snapshots are shown in figures 3-8.
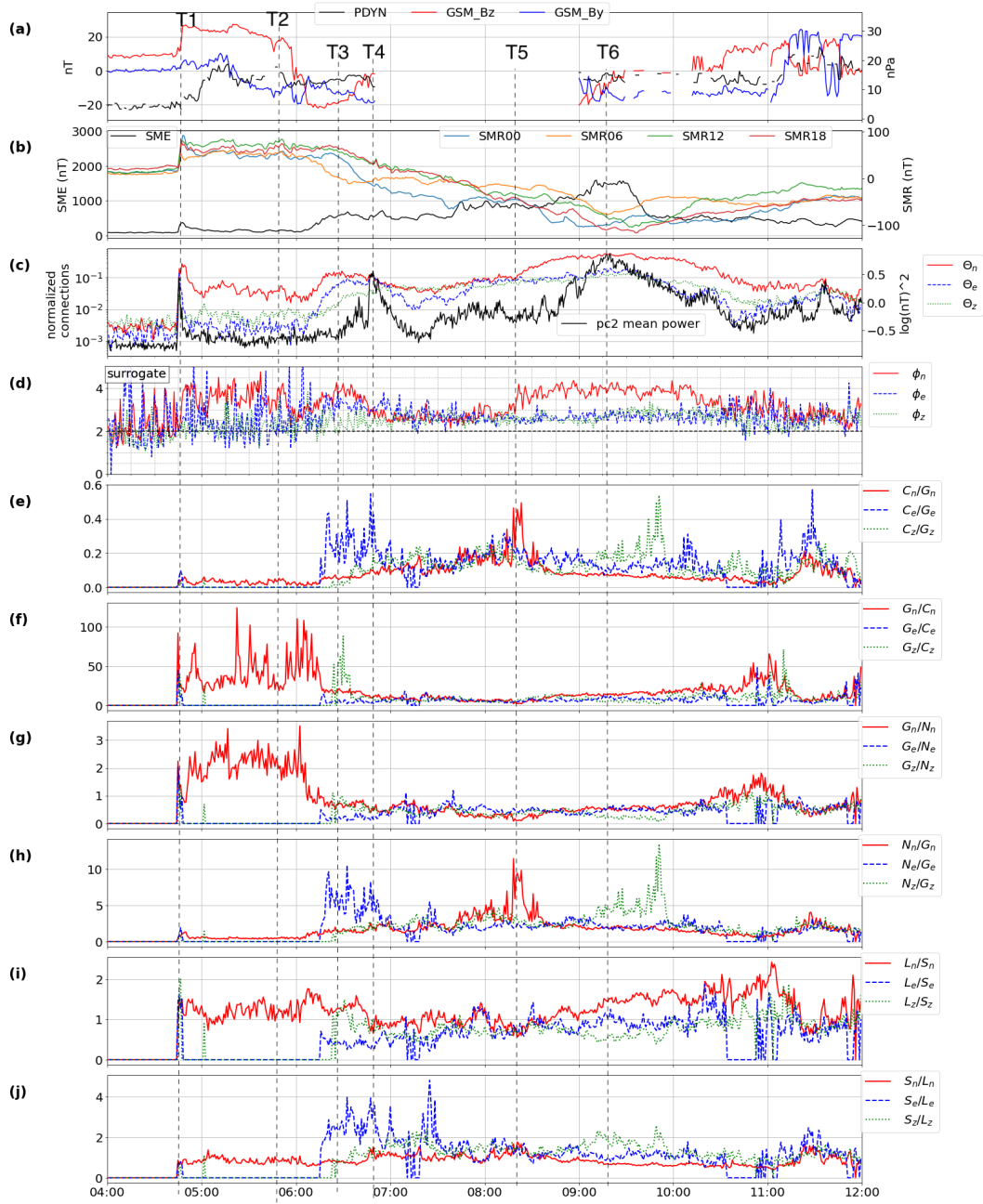
Figure 2: **Event overview and network parameters.** Panels (a)-(d) are as in figure 1. Panels (e)-(j), evolution of the undirected in-phase $\hat{n}$, $\hat{e}$, and $\hat{z}$ component network parameters which are ratios of the number of connections in the sub-networks discussed section 2.2 and their inverses. Panels (e) and (f), ratios between connections in northern and southern geomagnetic hemispheres (G_k) and magnetometer pseudo-chains (C_k). Panels (g) and (h), ratios between connections in the geomagnetic northern hemisphere (N_k) and connections between the geomagnetic northern and southern hemispheres (G_k). Panels (h) and (i), the proportion of connections less than 4 h in MLT (S_k) and greater than 4 h in MLT (L_k). Parameters are only plotted if the network has more than 100 connections, otherwise a value of zero is given. Reference times are labelled T1-6 for which network snapshots are shown in figures 3-8.
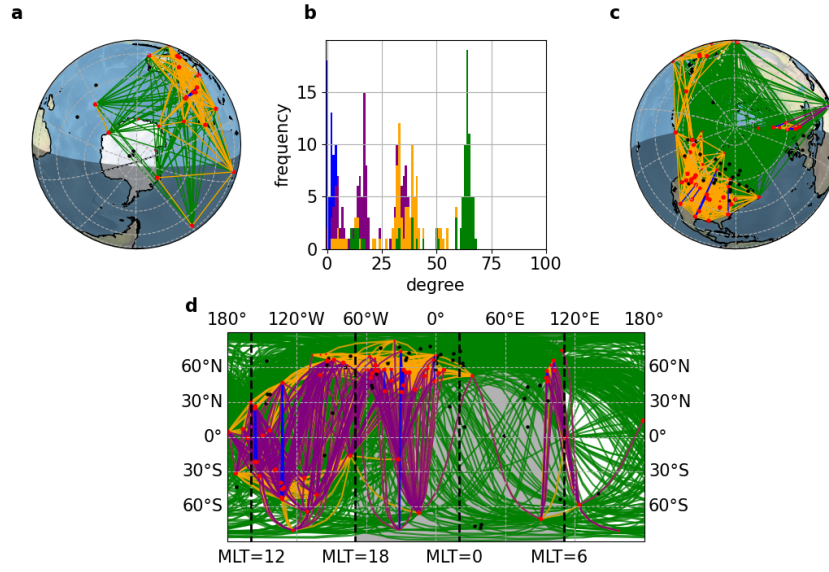
Figure 3: **Network snapshot at T1 (04:47:30 UT)** for the $\hat{n}$ magnetic field component comprising 81 stations. Throughout panels (a)-(d), all connections are plotted in green, over plotted with connections MLT <4 h in orange, while purple shows north-south connections with MLT <4 h, and blue connections for pseudo-chains. Panel (d) shows connections plotted in geomagnetic coordinates. Panels (a) and (b) show connections plotted in geographic coordinates and limited to the southern and northern hemispheres respectively. The global degree distribution for the given network snapshot is shown in (b) with colors corresponding to network edges in panels (a), (b), and (d).
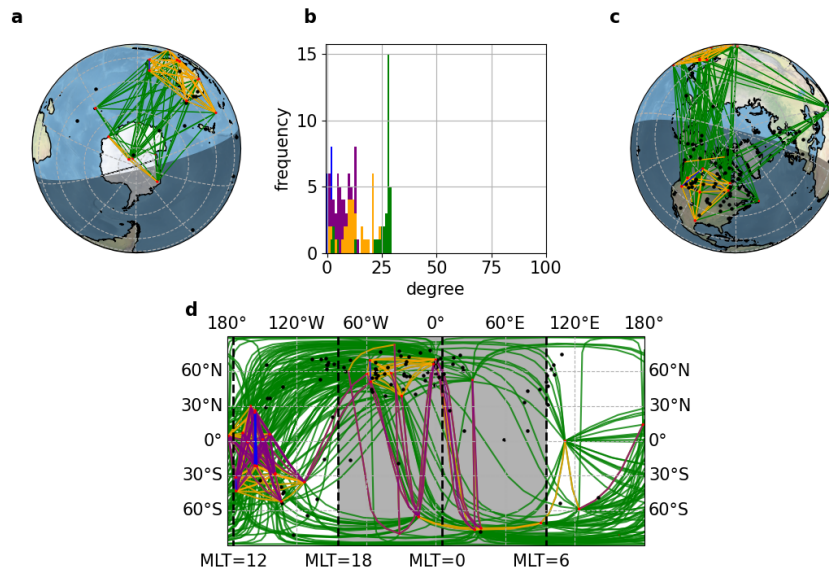
Figure 4: **Network snapshot at T2 (05:50:00 UT)** for the $\hat{n}$ magnetic field component network comprising 35 stations. The figure format is the same as figure 3.
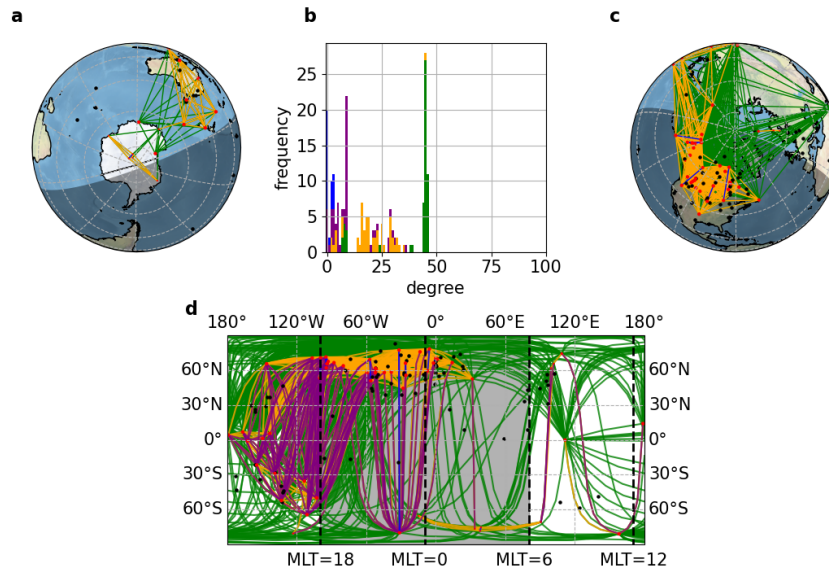
Figure 5: **Network snapshot at T3 (06:20:00 UT)** comprising 57 stations for the $\hat{n}$ component. The figure format is the same as figure 3.
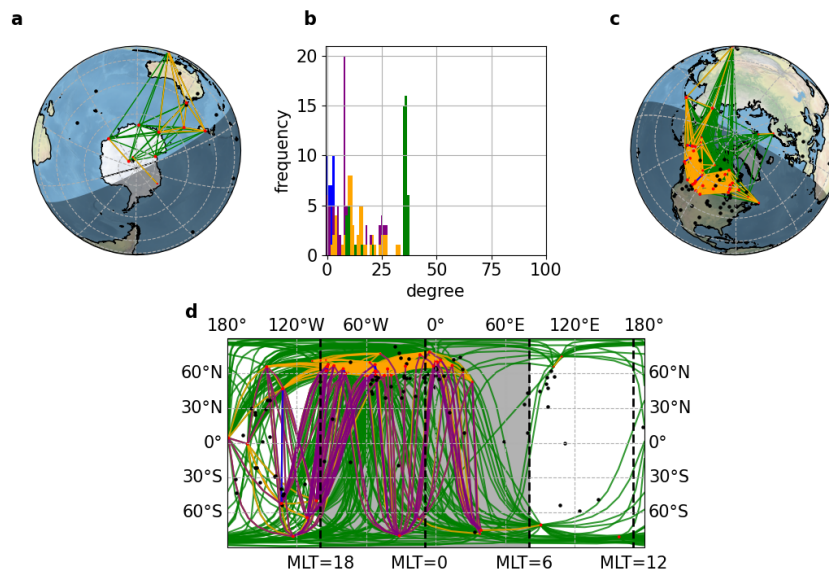
Figure 6: **Network snapshot at T4 (06:45:50 UT)** comprising 49 stations for the $\hat{n}$ component. The figure format is the same as figure 3.
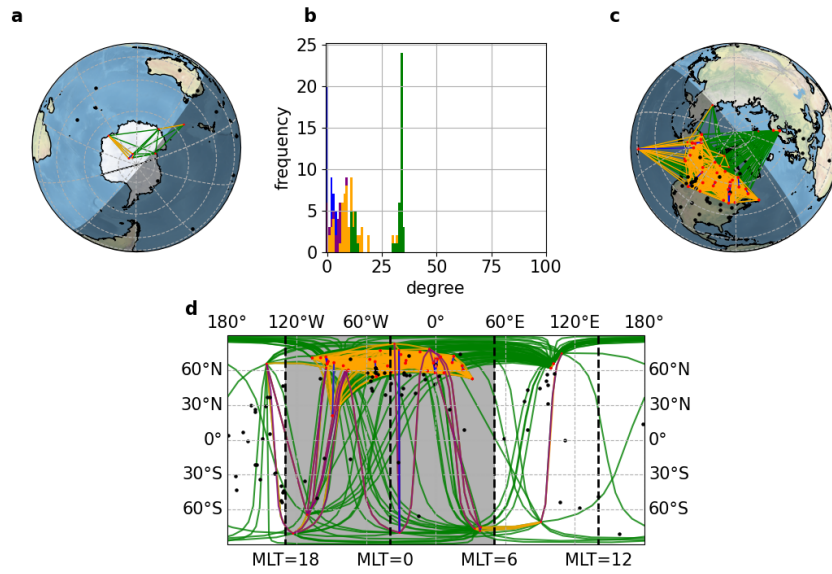
Figure 7: **Network snapshot at T5 (08:18:20 UT)** comprising 50 stations for the $\hat{n}$ component. The figure format is the same as figure 3.
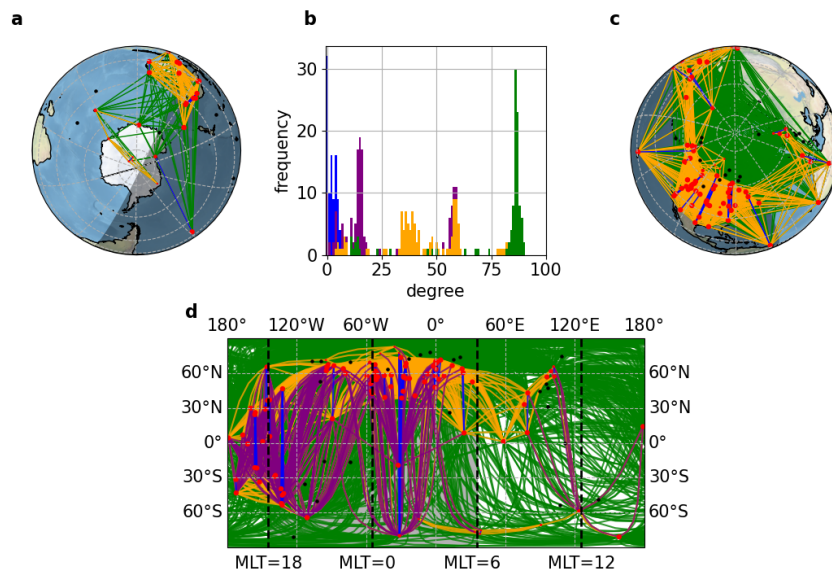

Figure 8: **Network snapshot at T6 (09:15:00 UT)** comprising 103 stations for the $\hat{n}$ component. The figure format is the same as figure 3.

We have provided a single event network analysis of the 2015 St. Patrick's Day storm for an 8 hour time window around onset. In the above results we have demonstrated that all the major phases of the storm are captured in network parameters, which are in turn derived from the dynamical network of Pc2 activity.

Other events analyzed include the 2013 St. Patrick's Day storm. Where we again find that the Pc2 in-phase networks are statistically significant for all magnetic field components over most of the event. We see a similar in-phase network and sub-network response at onset, however there are some deviations due to differences in solar wind driving conditions.

4 Discussion

There is a well developed literature of Pc wave studies focused on chains and geographically localized regions. One such example is the measurement of Pc1 and Pc5 waves during strong magnetospheric compression using the CRRES satellite and Scandinavian magnetometer chains on the dawn-side (Rasinkangas et al., 1994). In this paper we propose a new framework, namely networks, to quantify the dynamics of the global ULF activity from the full set of 100+ ground based magnetometers. This approach provides both detailed visualization, and quantitative parameterization of both locally and globally coherent ULF activity and the relationships between them. This first study is of an event that has already been subject to detailed analysis, the 2015 St. Patrick's Day storm. We characterize the globally coherent dynamical response of the magnetosphere as seen in Pc2 waves, reducing 128 time series to a few key network parameters. The network parameters that we propose here complement traditional geomagnetic indices which are designed to monitor specific larger scale current systems such as the auroral electrojet and ring current. This parameterization provides a starting point for statistical studies across multiple events which can discriminate between model predictions(Orr, Chapman, Gjerloev, & Guo, 2021).

Previously, 1 minute ground-magnetometer time resolution data has been used successfully to obtain the timings and structure of substorm current systems using network analysis techniques such as community detection (Dods et al., 2015; Orr et al., 2019; Orr, Chapman, Gjerloev, & Guo, 2021). Here, we construct the time dependent network using 1 second time resolution data which allows use to resolve the Pc wave response and to capture the evolution of geomagnetic storms in greater dynamical detail. The Pc2 wave band has a period between 5-10 seconds (Jacobs et al., 1964) and is the highest frequency Pc wave band resolvable with 1 second data, minimizing the length of the corresponding time window over which Fourier cross-correlation is estimated to form the network connections between station pairs.

We have focused principally on the $\hat{n}$ component, however networks are obtained for each of the magnetic field components, $\hat{n}$, $\hat{e}$ and $\hat{z}$ and these all respond at onset, but then behave differently throughout the storm. One clear example is seen in the sharp increase in northern hemisphere connections for the $\hat{e}$ component during SME enhancement at time T3 in figure 2, showing greater sensitivity to auroral electrojet formation. The evolution of geomagnetic storms in terms of the global coherence of Pc waves has a direct relation to the physics of the system. Standing Pc wave mode structure depends on the length of the field line and whether foot points move anti-phase or in-phase to each other (Hudson et al., 2004; Dai et al., 2013). For the closed field lines of the Earth's magnetic dipole, oscillations in the geomagnetic $\hat{e}$ component are in the toroidal direction, in the $\hat{n}$ component, poloidal, and the $\hat{z}$ component, approximately compressional.

In this first study we have shown that the instantaneous Pc2 networks, that is, constructed from cross correlation at zero lag, can categorize key phases in the 2015 St. Patrick's Day storm. There is also information contained in the non-zero lag cross correlation, which

can be used to track propagation of coherent Pc wave propagation by building directed networks. This will be the topic of future work.

5 Conclusions

In this paper we present a new methodology to build networks that capture the spatial coherence of global Pc2 wave activity. The time dependent network is constructed from 1 second observations using 100+ ground magnetometers collated by SuperMAG and Intermagnet. Our results show that the evolution of the 2015 St. Patrick's Day storm can be parameterized from the spatial extent and level of cross-correlation of Pc2 waves. The most significant response to the storm is found in the undirected in-phase network, where the cross correlation between Pc2 waveforms from pairs of magnetometers form peaks close to zero cross-correlation lag. However, the method has the potential to yield both undirected (cross-correlation lag close to zero) and directed (non-zero cross-correlation lag) networks corresponding respectively to an instantaneous and delayed, coherent response. We establish statistical significance of our results by testing against randomized surrogate data.

We identify a set of time dependent network parameters for field components $k = \hat{n}, \hat{e}, \hat{z}$ which track the phases of the storm as it evolves. These are:

- $C_k(t)/G_k(t)$ which is the number of connections within a restricted range of magnetic longitude normalized to the number of connections between the geomagnetic north and southern hemispheres. This parameterizes excitation along pseudo magnetometer chains, that is, across resonant field lines at localized MLT compared to the excitation globally across L shells.
- $G_k(t)/N_k(t)$ which is the number of connections between the geomagnetic northern and southern hemispheres normalized to connections in the geomagnetic northern hemisphere. This parameterizes local coherence versus global, L shell and closed field line spanning coherence and is also a flag for spatial undersampling, in this case the night-side response at high latitudes is seen for the St. Patrick's Day storm in the northern hemisphere as North America/Canada are located on the nightside.
- $S_k(t)/L_k(t)$ which is the number of connections between stations within MLT<4 h of each other normalized to the number of connections spanning MLT>4 h. This parameterizes excitation across magnetic L shells at a localized MLT compared to the excitation globally across L shells.

These network parameters respond to all the distinct phases of the storm, the initial onset, response to subsequent southward and northward turnings of the IMF, and enhancement of magnetospheric current systems seen in geomagnetic indices. The network response is based on cross-correlation and does not simply track the Pc2 wave power. We find a response to turnings of the IMF that are seen at 10-20 min delays, these precede enhancements in Pc2 wave power.

Once network parameters are established, they can be used to make detailed statistical comparisons across many events. This can quantify how the detailed evolution of a geomagnetic storm depends on the history of the solar wind driving, and the past state of the magnetosphere. This analysis can in principle also be applied and compared between different Pc wave bands as different Pc wave frequencies are generated by and respond to different solar/magnetospheric interactions.

Appendix A Building Dynamical Pc Wave Networks

Here we present the analysis process developed to build the dynamical Pc2 (or any other Pc wave) network in detail. The process requires two stages: (i) data preprocessing to extract the Pc2 waveforms from our raw data and (ii) constructing the network from the cross-correlation matrix formed between all possible station pairs.

A1 Pc Waveform Extraction

Before we can build networks, the data is preprocessed to extract the Pc waveforms, we summarize these steps shown in figure A1. For each magnetometer, a finite time interval is extracted at time t for a given magnetic field component, using a time window of $[t_k, t_k + 10T_{Pc_{max}}]$, where $T_{Pc_{max}}$ is the maximum value of the Pc wave period found in the window. Using a Tukey window in the time domain and overlapping successive windows such that time t is successively stepped by $t_{k+1} = t_k + 5T_{Pc_{max}}$, minimizes spectral leakage. Time windows containing more than $T_{Pc_{min}}/4$ of consecutive data gaps are excluded. The Pc wave mode is then extracted by band-pass filtering the FT of the windowed time series using the Butterworth filter (Butterworth et al., 1930) which has a frequency response which is relatively flat across the frequency band; we denote cut-off frequencies f_l, f_u (lower and upper frequency) and central frequency f_0. The time-domain Pc2 waveform is then obtained by IFT (Jacobs et al., 1964).
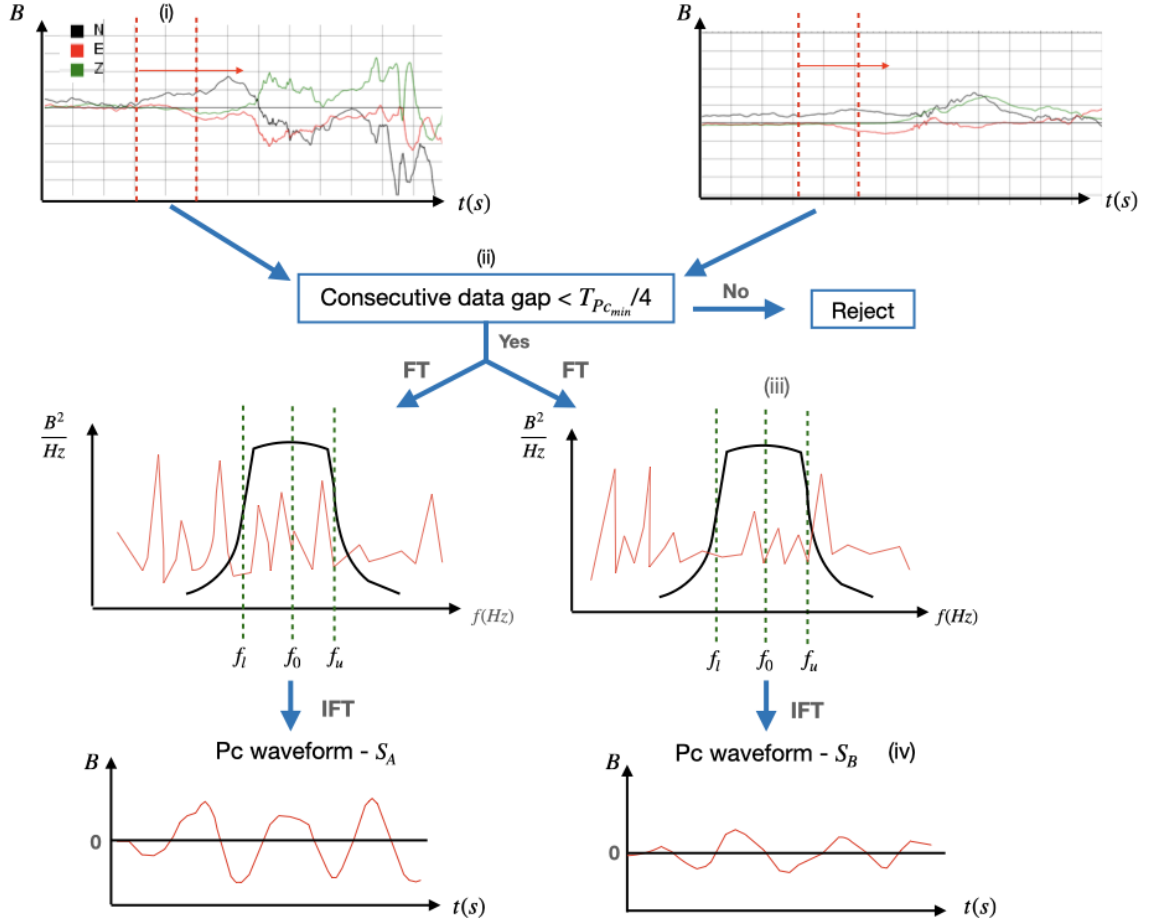
Figure A1: **Pc waveform extraction flow chart**. **(i)** Time window applied to a magnetic field component for two magnetometer station time series. **(ii)** If a time window has consecutive data gaps, reject and check the next pair of time windows. **(iii)** FT, then band-pass filter using a Butterworth filter for the desired Pc band. **(iv)** IFT to obtain the Pc waveforms.
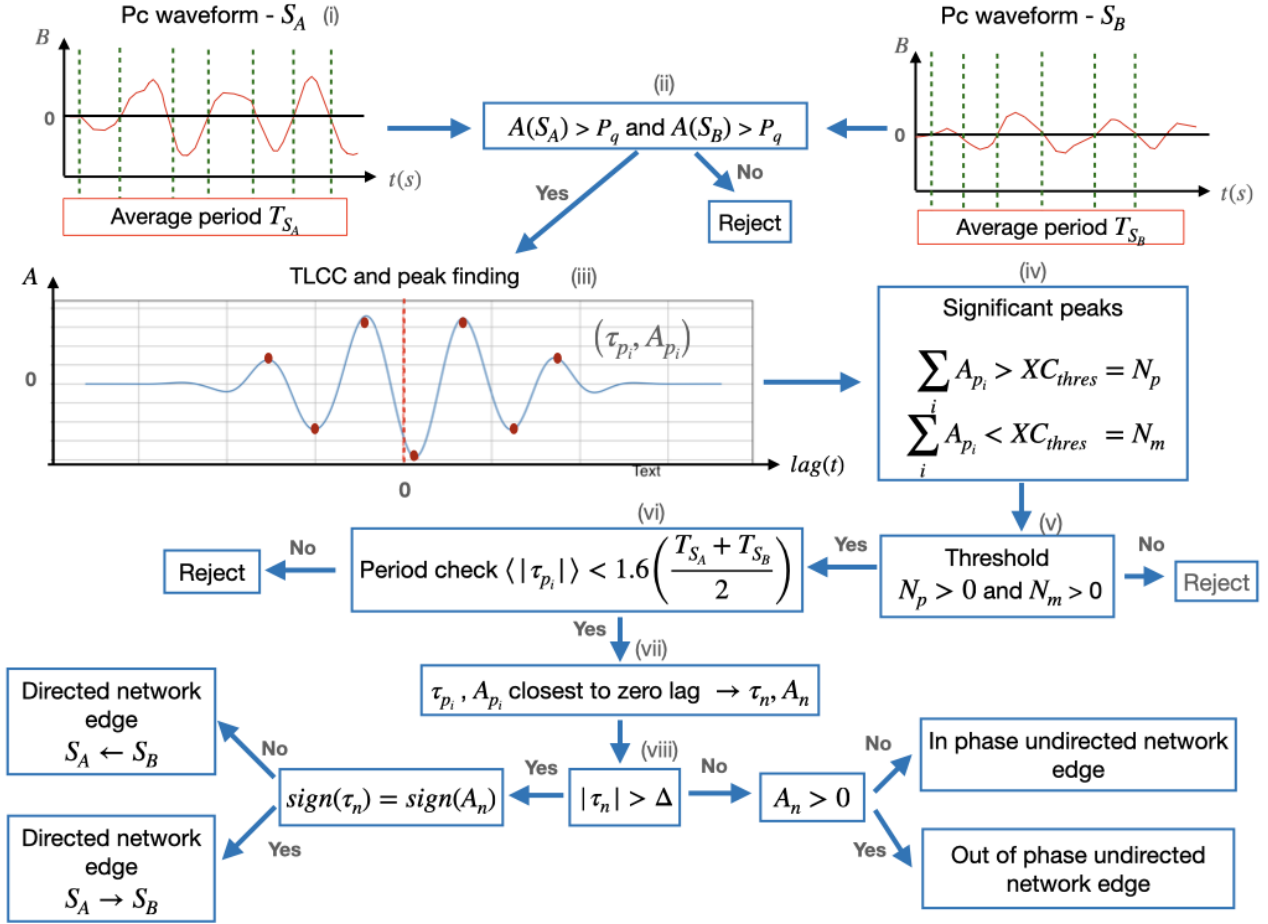
Figure A2: **Network edge building flow chart**. **(i)** Determine the average Pc waveform periods T_{S_A} and T_{S_B}. **(ii)** Reject Pc waveforms with amplitude below the average storm pre-onset levels. **(iii)** Obtain the TLCC between Pc waveforms S_A and S_B and find the extrema. **(iv)** Test the TLCC extrema exceed the modelled significance threshold. **(v)** Test that the modulus of both maxima and minima of the TLCC exceed the significance threshold. **(vi)** Test that the TLCC oscillation period is consistent with the average periods of its constituent waveforms. **(vii)** Determine the TLCC extremum closest to lag zero, A_n and lag τ_n. **(viii)** Amplitude A_n and lag τ_n classify the network connection between the two magnetometer stations as directed, undirected in-phase or undirected anti-phase.

A2 Constructing the Network

We obtain the time-lagged cross-correlation function (TLCC) between pairs of Pc waveforms extracted at each t_k for each field component and for each magnetometer station pair. The TLCC is used to determine whether a network edge, or connection exists between the pair magnetometer stations at each sample time t_k. We impose both a TLCC noise threshold and a waveform test, which are used to reject pairs of Pc waveforms where the TLCC is not statistically significant, as discussed below.

Pc waveforms that are above the noise are sinusoidal wave packets as they arise from a relatively narrow band-passed signal, the TLCC then oscillates as a function of lag, with the Pc waveform period. The lag τ_n, at which the TLCC has its maximum ex-

cursion nearest to zero lag, indicates whether the network connection is undirected ($|\tau_n| \leq 1$) or directed ($|\tau_n| > 1$). Depending whether the waveforms are instantaneously in-phase or anti-phase, we assign either an in-phase or anti-phase undirected connection. Directed connections arise when the pair of waveforms are maximally coherent when one of the waveforms is phase lagged w.r.t to the other. The sign of the non-zero lag indicates which signal is in advance of the other, hence the network connection has a direction.

The full procedure to build the network connections using Pc waveforms is detailed in Figure A2: (i) the zero crossings of Pc waveforms S_A and S_B are used to determine the average periods T_{S_A} and T_{S_B} **(ii)** The background noise threshold is set as $\sqrt{P_q}$, where $P(q)$ is the average quiet time power in the Pc2 wave band before onset. We require the peak values of both S_A and S_B to exceed this threshold. **(iii)** We obtain the TLCC between Pc waveforms S_A and S_B using the TLCC function (Pearson, 1896):

$$C_{X,Y}(\tau) = \frac{\sum_{t=1}^{N}(X(t) - \bar{X})(Y(t-\tau) - \bar{Y})}{(N-\tau)\sqrt{\frac{1}{N}\sum_{t=1}^{N}(X(t)-\bar{X})^2}\sqrt{\frac{1}{N}\sum_{t=1}^{N}(Y(t)-\bar{Y})^2}} \tag{A1}$$

the extrema of $C_{X,Y}(\tau)$ are determined using a standard peak finding routine. **(iv)** The threshold for the TLCC significance is set at 0.3, this threshold was obtained from test data of two sinusoidal signals superimposed with increasing amplitudes of white noise. **(v)** Waveforms are rejected unless both the maxima and minima of the TLCC exceeds this threshold **(vi)** Testing that the average period of the TLCC between the two waveforms is approximately equal to the average of the periods of the waveforms, to within a tolerance of a factor of 1.6, and reject waveforms that do not satisfy this criterion. **(vii)** Determine the amplitude A_n and lag τ_n of the TLCC peak closest to zero lag. **(viii)** A network connection (edge) is assigned between the two magnetometer stations for the time window used to obtain Pc waveforms, S_A and S_B. The type of connection is determined from the properties TLCC peak amplitude A_n and lag τ_n. If $|\tau_n| > 1$, the network connection is directed, the direction is determined by the sign of the lag τ_n. Otherwise if $|\tau_n| \leq 1$ and $A_n > 0$ the network connection is in-phase and undirected, whereas if $A_n < 0$ the network connection is anti-phase and undirected.

Appendix B Anti-phase Network Response

The anti-phase response to the 2015 St. Patrick's Day storm is detailed in figures B1 and B2. At onset only the $\hat{n}$ component network is significant ($\phi_k > 2$), for which we see a response in all sub-networks, similar to the in-phase network response. All connections $\hat{n}$, $\hat{e}$ and $\hat{z}$ become significant from 06:45 - 08:15 UT. Approximately 30 minutes after the Pc2 power peak at 06:45:00 UT, we see an enhancement in connections between the northern and southern geomagnetic hemispheres relative to geomagnetic northern hemisphere connections, as $G_e/N_e > 1$ and corresponding to an increase in long-range connections as $L_e/S_e > 1$. From 08:15:00 - 10:15:00 UT only the $\hat{e}$ and $\hat{z}$ components are significant and short-range and northern hemisphere connections are enhanced for the $\hat{z}$ component as $N_z/G_z > 1$ and $S_z/L_z > 1$, when SME and Pc2 power peak, while SMR by MLT is close to minimum. Similarly to the in-phase networks, the number of sub-network connections reaches a peak at this time. An enhancement in northern hemisphere connections for the $\hat{z}$ component in-phase network is seen 35 minutes after the anti-phase response, with $N_z/G_z > 1$.
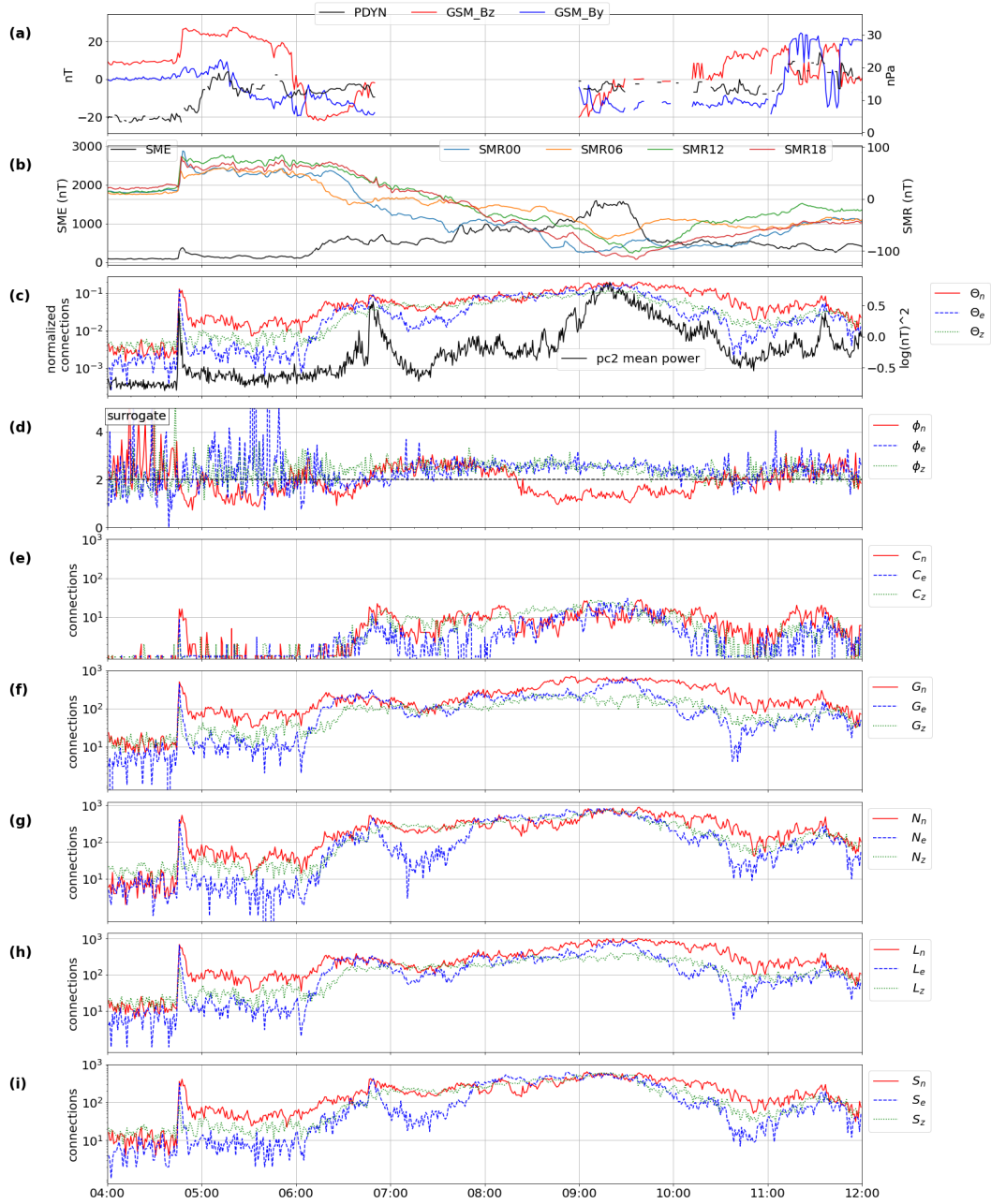
Figure B1: **Event overview and anti-phase sub-networks.** The panels (a)-(d) have the same format as figure 1.
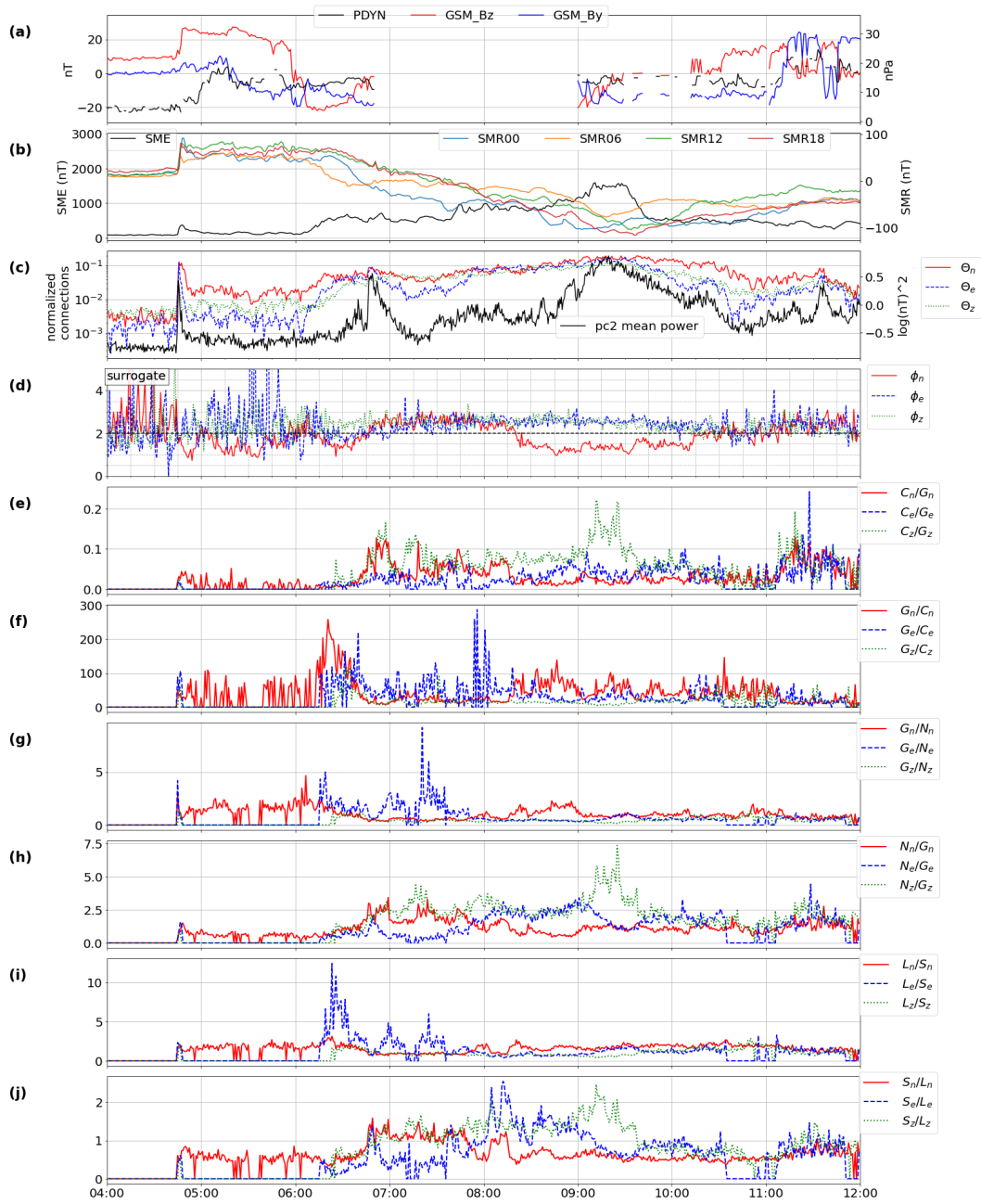
Figure B2: **Event overview and anti-phase network parameters.** The panels (a)-(j) have the same format as figure 2.

Appendix C In-phase Network Snapshots

Here we show the in-phase network snapshots for the $\hat{e}$ and $\hat{z}$ component networks, where these networks have different behaviour to the $\hat{n}$ component network and have significant edges, figures C1-5. To compare component network snapshots we will use reference times T1-6 as seen in figures 3-8. At time T4, the Pc2 power spikes and the $\hat{e}$ component network has a lower number of north-south (purple) connections as compared to the $\hat{n}$ component network. However at T5, the $\hat{e}$ and $\hat{z}$ component networks have more north-south connections than the $\hat{n}$ component network. The $\hat{e}$ component network at T5 has two distinct northern hemisphere clusters for connections limited to MLT<4 h. Later at T6, the number of connections for all networks components is maximum and the degree distribution for $\hat{e}$ component sub-networks in figure C4, panel (d) is broader with a lower average degree than the $\hat{n}$ component network. Compared to the global activity seen in the $\hat{n}$ component network snapshot at T6 the $\hat{z}$ component network shows northern hemisphere (North American) connections dominate.
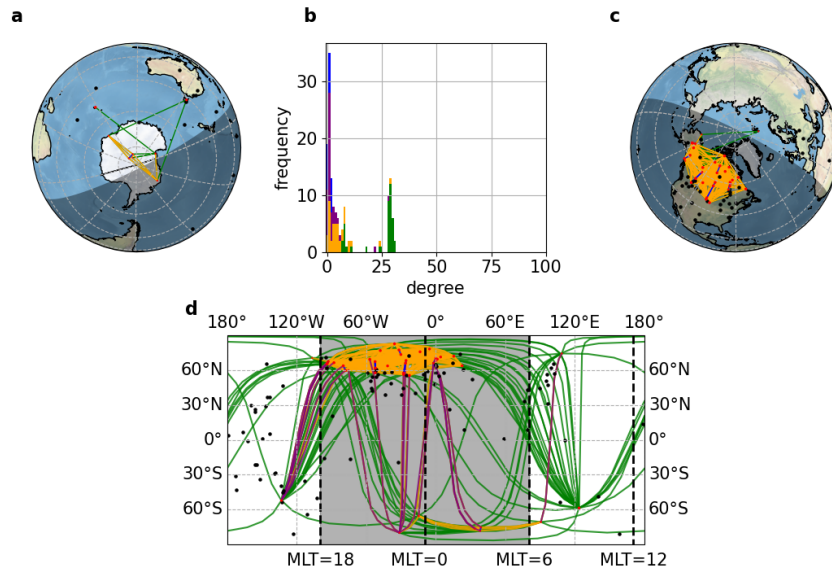
Figure C1: **Network snapshot at T4 (06:45:50 UT)** comprising 41 stations for the $\hat{e}$ component. The figure format is the same as figure 3.
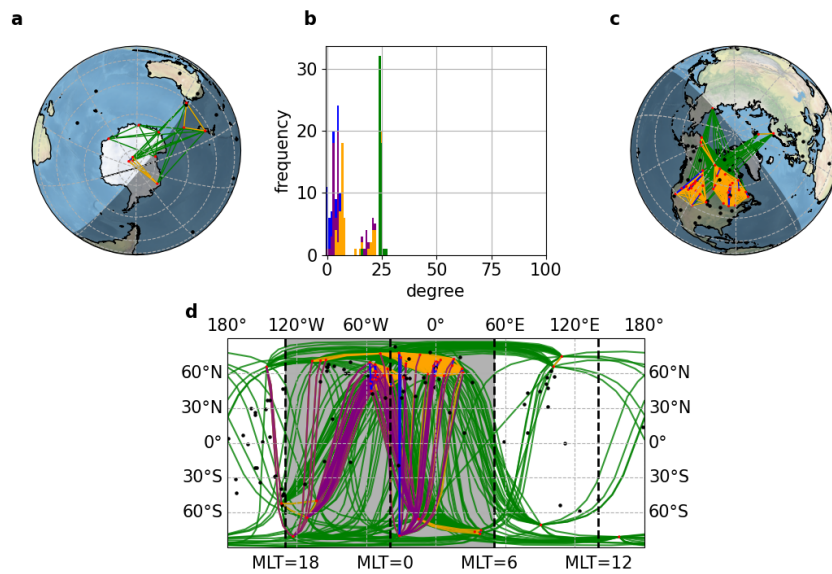

Figure C2: **Network snapshot at T5 (08:18:00 UT)** comprising 53 stations for the $\hat{e}$ component network. The figure format is the same as figure 3.
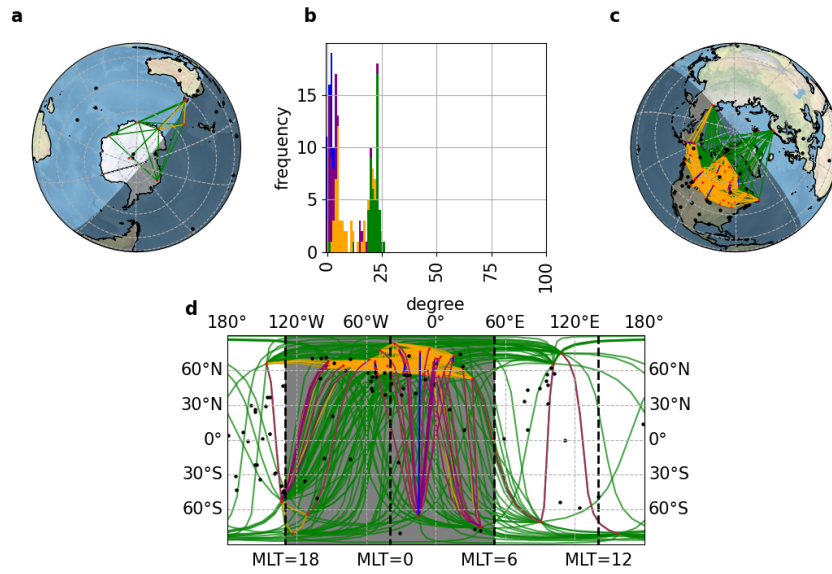
Figure C3: **Network snapshot at T5 (08:18:50 UT)** comprising 49 stations for the $\hat{z}$ component network. The figure format is the same as figure 3.
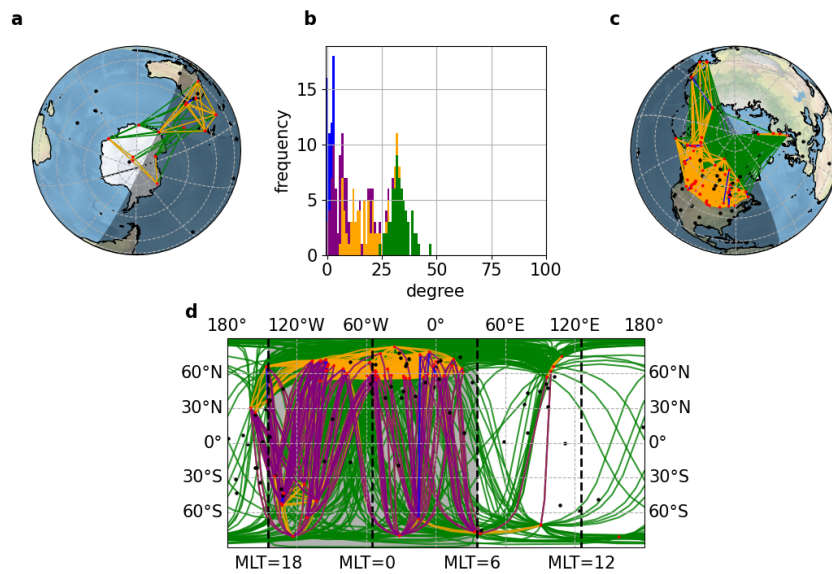

Figure C4: **Network snapshot at T6 (09:15:00 UT)** comprising 67 stations for the $\hat{e}$ component network. The figure format is the same as figure 3.
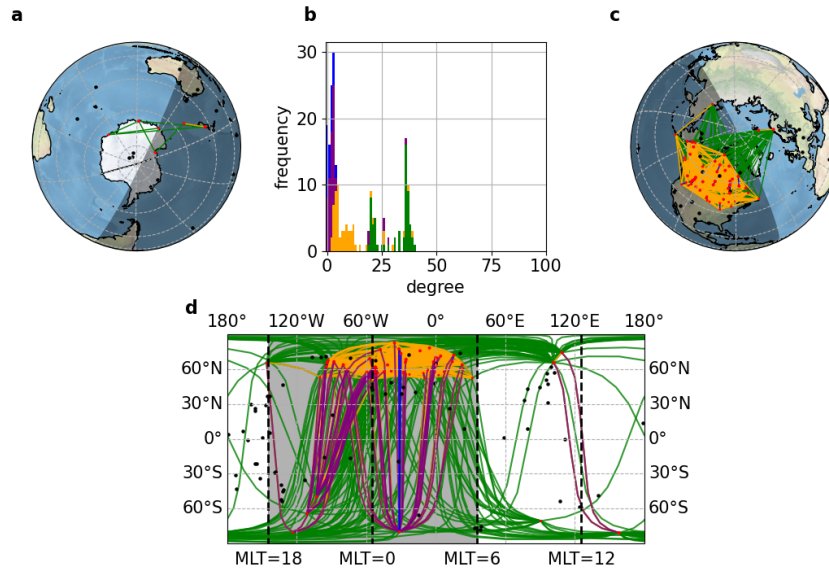
Figure C5: **Network snapshot at T6 (09:15:00 UT)** comprising 61 stations for the $\hat{z}$ component network. The figure format is the same as figure 3.

References

Arnoldy, R., Engebretson, M., Alford, J., Erlandson, R., & Anderson, B. (1996). Magnetic impulse events and associated Pc 1 bursts at dayside high latitudes. *Journal of Geophysical Research: Space Physics*, *101*(A4), 7793–7799.

Baumjohann, W., & Treumann, R. A. (2012). *Basic space plasma physics.* World Scientific Publishing Company.

Boccaletti, S., Latora, V., Moreno, Y., Chavez, M., & Hwang, D.-U. (2006). Complex networks: Structure and dynamics. *Physics reports*, *424*(4-5), 175–308.

Butterworth, S., et al. (1930). On the theory of filter amplifiers. *Wireless Engineer*, *7*(6), 536–541.

Chisham, G., & Orr, D. (1997). A statistical study of the local time asymmetry of Pc 5 ULF wave characteristics observed at midlatitudes by samnet. *Journal of Geophysical Research: Space Physics*, *102*(A11), 24339–24350.

Clilverd, M. A., Rodger, C. J., Kamp, M. V. D., & Verronen, P. T. (2020). Electron precipitation from the outer radiation belt during the st. patrick's day storm 2015: Observations, modeling, and validation. *Journal of Geophysical Research: Space Physics*. doi: 10.1029/2019JA027725

Dai, L., Takahashi, K., Wygant, J. R., Chen, L., Bonnell, J., Cattell, C. A., . . .

others (2013). Excitation of poloidal standing alfvén waves through drift resonance wave-particle interaction. *Geophysical Research Letters*, *40*(16), 4127–4132.

Dods, J., Chapman, S., & Gjerloev, J. (2015). Network analysis of geomagnetic substorms using the SuperMAG database of ground-based magnetometer stations. *Journal of Geophysical Research: Space Physics*, *120*(9), 7774–7784.

Dods, J., Chapman, S., & Gjerloev, J. (2017). Characterizing the ionospheric current pattern response to southward and northward imf turnings with dynamical SuperMAG correlation networks. *Journal of Geophysical Research: Space Physics*, *122*(2), 1883–1902.

Engebretson, M., Lessard, M., Bortnik, J., Green, J., Horne, R. B., Detrick, D., . . . others (2008). Pc1–Pc2 waves and energetic particle precipitation during and after magnetic storms: Superposed epoch analysis and case studies. *Journal of Geophysical Research: Space Physics*, *113*(A1).

Gjerloev, J. (2012). The SuperMAG data processing technique. *Journal of Geophysical Research: Space Physics*, *117*(A9).

Gonzalez, W., Joselyn, J.-A., Kamide, Y., Kroehl, H. W., Rostoker, G., Tsurutani, B., & Vasyliunas, V. (1994). What is a geomagnetic storm? *Journal of Geophysical Research: Space Physics*, *99*(A4), 5771–5792.

Hudson, M., Denton, R., Lessard, M., Miftakhova, E., & Anderson, R. (2004). A study of Pc-5 ULF oscillations. In *Annales geophysicae* (Vol. 22, pp. 289–302).

Hughes, W. J. (2013, 4). Magnetospheric ULF waves: A tutorial with a historical perspective. , 1-11. doi: 10.1029/GM081P0001

Jacobs, J., Kato, Y., Matsushita, S., & Troitskaya, V. (1964). Classification of geomagnetic micropulsations. *Journal of Geophysical Research*, *69*(1), 180–181.

Jacobsen, K. S., & Andalsvik, Y. L. (2016). Overview of the 2015 st. patrick's day storm and its consequences for rtk and ppp positioning in norway. *Journal of Space Weather and Space Climate*, *6*, A9.

Kitamura, T.-i., Saka, O., Shimoizumi, M., Tachihara, H., Oguti, T., ARAKI, T., . . . Nyobe, J. (1988). Global mode of pi2 waves in the equatorial region difference of pi2 mode between high and equatorial latitudes. *Journal of geomagnetism and geoelectricity*, *40*(5), 621–634.

Kozyra, J., Jordanova, V., Home, R., & Thorne, R. (1997). Modeling of the contribution of electromagnetic ion cyclotron (emic) waves to stormtime ring current erosion. *Washington DC American Geophysical Union Geophysical Monograph Series*, *98*, 187–202.

Li, Z., Hudson, M., Patel, M., Wiltberger, M., Boyd, A., & Turner, D. (2017). ULF wave analysis and radial diffusion calculation using a global mhd model for the 17 march 2013 and 2015 storms. *Journal of Geophysical Research: Space Physics*, *122*(7), 7353–7363.

Mahrous, A. M., Ibrahim, M., Berdermann, J., & Salah, H. M. (2018, 12). Ionospheric scintillations detected by scinda-helwan station during st. patrick's day geomagnetic storm. *NRIAG Journal of Astronomy and Geophysics*, *7*, 214-219. doi: 10.1016/J.NRJAG.2018.05.007

Maurya, A. K., Venkatesham, K., Kumar, S., Singh, R., Tiwari, P., & Singh, A. K. (2018, 8). Effects of st. patrick's day geomagnetic storm of march 2015 and of june 2015 on low-equatorial d region ionosphere. *Journal of Geophysical Research: Space Physics*, *123*, 6836-6850. doi: 10.1029/2018JA025536

McGranaghan, R. M., Mannucci, A. J., Verkhoglyadova, O., & Malik, N. (2017). Finding multiscale connectivity in our geospace observational system: Network analysis of total electron content. *Journal of Geophysical Research: Space Physics*, *122*(7), 7683–7697.

McPherron, R., Russell, C., & Coleman, P. (1972). Fluctuating magnetic fields in the magnetosphere. *Space Science Reviews*, *13*(3), 411–454.

Menk, F. W. (2011). Magnetospheric ULF waves: A review. In *The dynamic magne-

tosphere (pp. 223–256). Springer.

Moen, J., Hosokawa, K., Gulbrandsen, N., & Clausen, L. B. N. (2015). On the symmetry of ionospheric polar cap patch exits around magnetic midnight. *Journal of Geophysical Research: Space Physics*, *120*(9), 7785–7797.

Murphy, K. R., Mann, I. R., & Ozeke, L. G. (2014). A ULF wave driver of ring current energization. *Geophysical Research Letters*, *41*(19), 6595–6602.

Newell, P., & Gjerloev, J. (2012). SuperMAG-based partial ring current indices. *Journal of Geophysical Research: Space Physics*, *117*(A5).

Newman, M. (2018). *Networks*. Oxford university press.

Nosé, M., Iyemori, T., Wang, L., Hitchman, A., Matzka, J., Feller, M., . . . others (2012). Wp index: A new substorm index derived from high-resolution geomagnetic field data at low latitude. *Space Weather*, *10*(8), 1–12.

Orr, L., Chapman, S., & Beggan, C. (2021). Wavelet and network analysis of magnetic field variation and geomagnetically induced currents during large storms. *Space Weather*, *19*(9), e2021SW002772.

Orr, L., Chapman, S., & Gjerloev, J. (2019). Directed network of substorms using SuperMAG ground-based magnetometer data. *Geophysical Research Letters*, *46*(12), 6268–6278.

Orr, L., Chapman, S., Gjerloev, J., & Guo, W. (2021). Network community structure of substorms using SuperMAG magnetometers. *Nature communications*, *12*(1), 1–10.

Pearson, K. (1896). Vii. mathematical contributions to the theory of evolution.—iii. regression, heredity, and panmixia. *Philosophical Transactions of the Royal Society of London. Series A, containing papers of a mathematical or physical character*(187), 253–318.

Poppe, B. B. (2000). New scales help public, technicians understand space weather. *Eos, Transactions American Geophysical Union*, *81*(29), 322–328.

Pulkkinen, T. (2007). Space weather: terrestrial perspective. *Living Reviews in Solar Physics*, *4*(1), 1.

Rasinkangas, R., Mursula, K., Kremser, G., Singer, H., Fraser, B., Korth, A., & Hughes, W. (1994). Simultaneous occurrence of Pc 5 and Pc 1 pulsations in the dawnside magnetosphere: Crres observations. *Geophysical Monograph-American Geophysical Union*, *81*, 417–417.

Schreiber, T., & Schmitz, A. (2000). Surrogate time series. *Physica D: Nonlinear Phenomena*, *142*(3-4), 346–382.

Schwenn, R. (2006). Space weather: The solar perspective. *Living reviews in solar physics*, *3*(1), 2.

Southwood, D., & Hughes, W. (1983). Theory of hydromagnetic waves in the magnetosphere. *Space Science Reviews*, *35*(4), 301–366.

Strogatz, S. H. (2001). Exploring complex networks. *nature*, *410*(6825), 268–276.

Todd, H., Cowley, S., Lockwood, M., Willis, D., & Lühr, H. (1988). Response time of the high-latitude dayside ionosphere to sudden changes in the north-south component of the imf. *Planetary and Space Science*, *36*(12), 1415–1428.

Wu, C. C., Liou, K., Lepping, R. P., Hutting, L., Plunkett, S., Howard, R. A., & Socker, D. (2016a, 12). The first super geomagnetic storm of solar cycle 24: "the st. patrick's day event (17 march 2015)" global data systems for the study of solar-terrestrial variability. *Earth, Planets and Space*, *68*, 1-12. doi: 10.1186/S40623-016-0525-Y

Wu, C.-C., Liou, K., Lepping, R. P., Hutting, L., Plunkett, S., Howard, R. A., & Socker, D. (2016b). The first super geomagnetic storm of solar cycle 24: "the st. patrick's day event (17 march 2015)". *Earth, Planets and Space*, *68*(1), 1–12.

Yumoto, K. (1988). External and internal sources of low-frequency mhd waves in the magnetosphere-a review. *Journal of geomagnetism and geoelectricity*, *40*(3), 293–311.

743   Ziesolleck, C., & McDiarmid, D. (1994). Auroral latitude Pc 5 field line resonances:
744   Quantized frequencies, spatial characteristics, and diurnal variation. *Journal of*
745   *Geophysical Research: Space Physics*, *99*(A4), 5817–5830.